

Synthesis, Growth, and Er^{3+} Luminescence of Lanthanide Phosphate Nanoparticles[†]

O. Lehmann, H. Meyssamy, K. Kömpe, H. Schnablegger, and M. Haase*

Institut für Physikalische Chemie, Universität Hamburg, Bundesstraße 45, D-20146 Hamburg, Germany

Received: January 8, 2003

The complete series of all nonradioactive lanthanide phosphates has been prepared in organic solution as ligand-capped nanoparticles. In all cases, well-dispersed particles with mean sizes below 10 nm are obtained. Despite the similar chemical properties of the lanthanides, the growth, the crystal structure, and the mean size of the nanocrystals are found to be strongly affected by the lanthanide ion employed. Very small nanoparticles are obtained for lanthanides for which the lattice energies of the bulk tetragonal xenotime phase and the bulk monoclinic monazite phase are similar. These smaller nanoparticles do not show the expected phase transition from monoclinic to tetragonal and seem to have their own unique crystal structure. Possible explanations for these observations are discussed. Finally, we present the first results on the IR emission of Er^{3+} -doped YbPO_4 and $(\text{Lu}, \text{Yb})\text{PO}_4$ nanoparticles in solution.

Introduction

The lanthanide phosphates form a class of chemically stable materials that have been considered, for instance, to be host materials for the long-term encapsulation of trivalent actinides contained in radioactive waste. Terbium-doped lanthanum cerium phosphate is commercially available as the green emitter in fluorescent lamps because it combines high luminescence efficiency with high chemical resistance in the presence of a mercury discharge.¹

Recently, we have shown that doped lanthanum and cerium phosphates can be prepared as nanoparticles in gram amounts in high-boiling coordinating solvents² and that dopant ions introduced into the nanocrystalline lattice occupy lattice sites identical to those of the corresponding bulk material.³ Moreover, these nanoparticles can have high luminescence quantum yields despite their small size of about 6 nm. Because these particles can be easily dispersed without agglomeration in a variety of solvents and because their nanocrystalline lattice provides a rigid crystal environment for dopant ions, these systems combine the high solubility of organic laser dyes or organometallic complexes with the advantages of solid-state hosts. Therefore, these particles may be of interest as components in a variety of applications.^{4,5} Doping of these nanocrystalline hosts with lanthanide ions is, of course, not restricted to ions that emit in the UV–vis region. Also, IR-emitting lanthanide ions such as Nd^{3+} , Yb^{3+} or Er^{3+} may be introduced into the lattice, as has been described recently in a patent⁴ and by van Veggel et al.⁵

Although the doping of different ions into lanthanum or cerium phosphate nanoparticles is straightforward, the synthesis given in ref 2 is not optimal for the preparation of pure phosphate nanoparticles of the heavier lanthanides. In this paper, we present a modified synthesis that can be applied equally well to all rare earth ions. We used this method to prepare the whole series of lanthanide phosphate nanoparticles with the exception of promethium phosphate, the latter of which is radioactive. Owing to the high chemical similarity of the lanthanide ions, this series provides the unique opportunity to study the influence

of subtle differences in the ionic radii on the growth of nanoparticles.

Finally, we show that YbPO_4 and LuPO_4 nanoparticles, both showing the tetragonal lattice structure rather than the monoclinic structure of the lighter lanthanides, can be successfully doped with Er^{3+} .

Experimental Section

Lanthanide phosphate nanoparticles were prepared in organic solution according to the following procedure.⁴ A clear solution of a hydrated lanthanide trichloride (10 mmol) in approximately 10 mL of methanol p.a. was mixed with tributyl phosphate (20 mmol), and the methanol was subsequently removed with a rotary evaporator. Diphenyl ether (30 mL) was added, and the water, released by the metal chloride, was distilled off under vacuum at 50–80 °C. Subsequently, 30 mmol of trihexylamine and 7.0 mL of a 2 M solution of dry phosphoric acid in dihexyl ether were added, and the mixture was heated to 200 °C under dry nitrogen. After 2 h, heating was stopped, and the reaction mixture was allowed to cool. Clear colloids of lanthanide phosphate nanoparticles were obtained, except for the heavier elements La^{3+} , Ce^{3+} , Pr^{3+} , and Nd^{3+} , the solutions of which are slightly turbid. This turbidity can be avoided by employing 40 mmol of tributyl phosphate (rather than 20 mmol) in these cases. After the diphenyl ether has been removed by vacuum distillation at 100 °C, the viscous residue was dissolved in approximately 300 mL of methanol, and the mixture was loaded into a stirring (diafiltration) cell (Berghof) equipped with a 5000-Da filter (Millipore). Using a nitrogen pressure of 5–6 bar, the solution was passed through the filter until the volume of the solution was reduced to 50 mL. The remaining cell contents were mixed with 300 mL of methanol and passed again through the filter. After repeating this procedure five times, the nanoparticles were isolated from the purified colloid by removing the methanol with a rotary evaporator.

As-prepared nanoparticles can be easily redispersed at room temperature in 2-propanol containing some tetrabutylammonium hydroxide or in dodecylamine at 200 °C. Nanoparticles that are highly soluble in apolar solvents are obtained by diluting the dodecylamine solution (at about 50 °C) with toluene, precipitat-

[†] Part of the special issue "Arnim Henglein Festschrift".

* Corresponding author. E-mail: hasse@chemie.uni-hamburg.de.

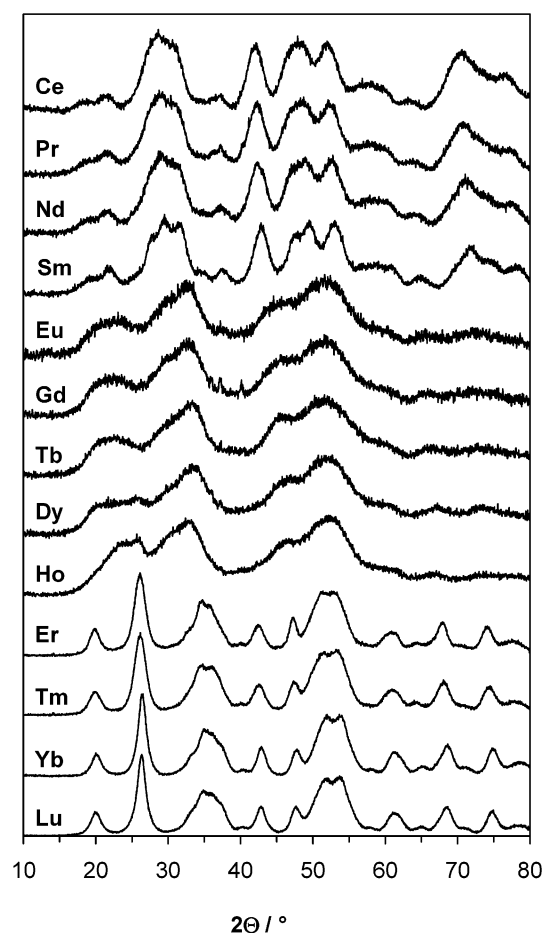


Figure 1. X-ray powder diffraction data of the series of lanthanide phosphate nanoparticles.

ing the nanoparticles with methanol, washing the precipitate two times with methanol, and finally, drying the nanoparticles at room temperature.

X-ray diffraction patterns of powder samples were recorded with a Philips X'pert system. UV–vis absorption and IR-photoluminescence spectra of the colloidal solutions were measured with a Cary 500 Scan spectrometer (Varian) and a Fluorolog III spectrometer (Jobin Yvon) equipped with a liquid-nitrogen-cooled germanium detector (Northcoast), respectively.

The size and the agglomeration of nanoparticles in solution was investigated by small-angle X-ray scattering (SAXS) experiments (Kratky compact camera). By assuming the scatterers to be homogeneous spheres, the size distribution was calculated from the scattering curve by means of the indirect transformation method^{6–8} (ITP software, University of Graz, Austria).

High-resolution electron micrographs of the particles were taken using a Philips CM 300 UT transmission electron microscope (TEM) operating at an acceleration voltage of 300 kV. The microscope was equipped with a CCD camera (Gatan, model no. 694).

Results and Discussion

The synthesis procedure described in the Experimental Section has been employed for all lanthanide phosphates and yields gram amounts of redispersible nanoparticles in all cases. Figure 1 shows the X-ray powder diffraction data of these nanomaterials. In all cases, the width of the diffraction lines is strongly broadened because of the small size of the crystallites.

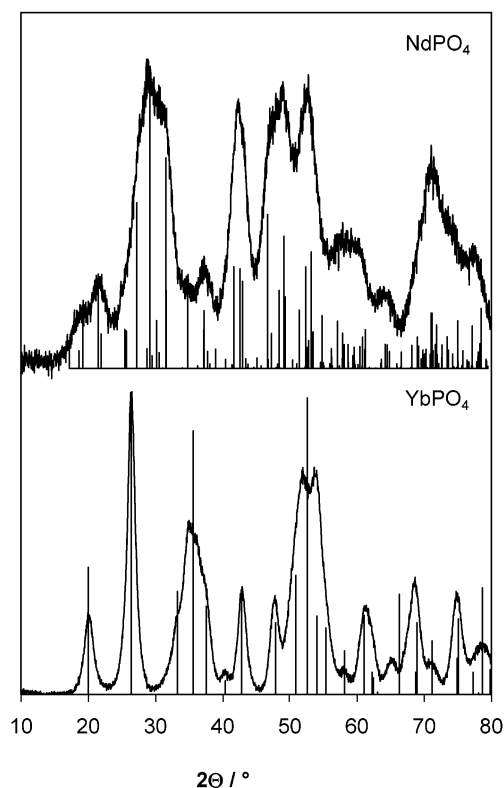


Figure 2. XRD data of powders of neodymium phosphate nanocrystals (top) and of ytterbium phosphate nanocrystals (bottom), including line spectra of the corresponding bulk materials. The crystal structure is monazite type for NdPO_4 (monoclinic, PDF no. 78-1167) and xenotime (zircon) type for YbPO_4 (tetragonal, PDF no. 83-664).

Three different types of diffraction patterns are observed. Phosphate nanoparticles of the lighter lanthanides cerium, praseodymium, neodymium, and samarium display very similar diffractograms with peak positions and intensities in accord with the monoclinic monazite phase of the corresponding bulk materials (Figure 1 and top part of Figure 2).⁹ Similar diffractograms were observed earlier for doped lanthanum phosphate nanoparticles.³ Diffractograms that are very different from those of the lighter lanthanides are observed for the phosphates of the heavy lanthanides erbium, thulium, ytterbium, and lutetium. The line positions in the patterns of these four elements are very similar and are in accord with the tetragonal xenotime phase known from the corresponding bulk phosphates (bottom part of Figure 2).⁹ From both types of diffractograms, the mean particle size can be estimated by using the Debye–Scherrer formula, yielding mean particle diameters between 4 and 7 nm for all systems. These values are in accord with the mean sizes determined from TEM images of the phosphate nanoparticles (Figure 3). The TEMs of cerium, praseodymium, neodymium, and samarium phosphate nanoparticles, all crystallizing in the monazite structure, show very similar particle shapes and sizes. The top part of Figure 3 shows neodymium phosphate nanoparticles as an example. Similar observations are made for the lanthanide phosphates that crystallize in the xenotime structure. Erbium, thulium, ytterbium, and lutetium phosphate nanoparticles show almost identical TEM images; the bottom part of Figure 3 displays an image of ytterbium phosphate particles.

The transition of the crystal phase from monoclinic to tetragonal is caused by the decrease in the ionic radius from cerium to lutetium. For the bulk materials, the monoclinic phase is observed from cerium phosphate to gadolinium phosphate whereas tetragonal lattices are observed from dysprosium to

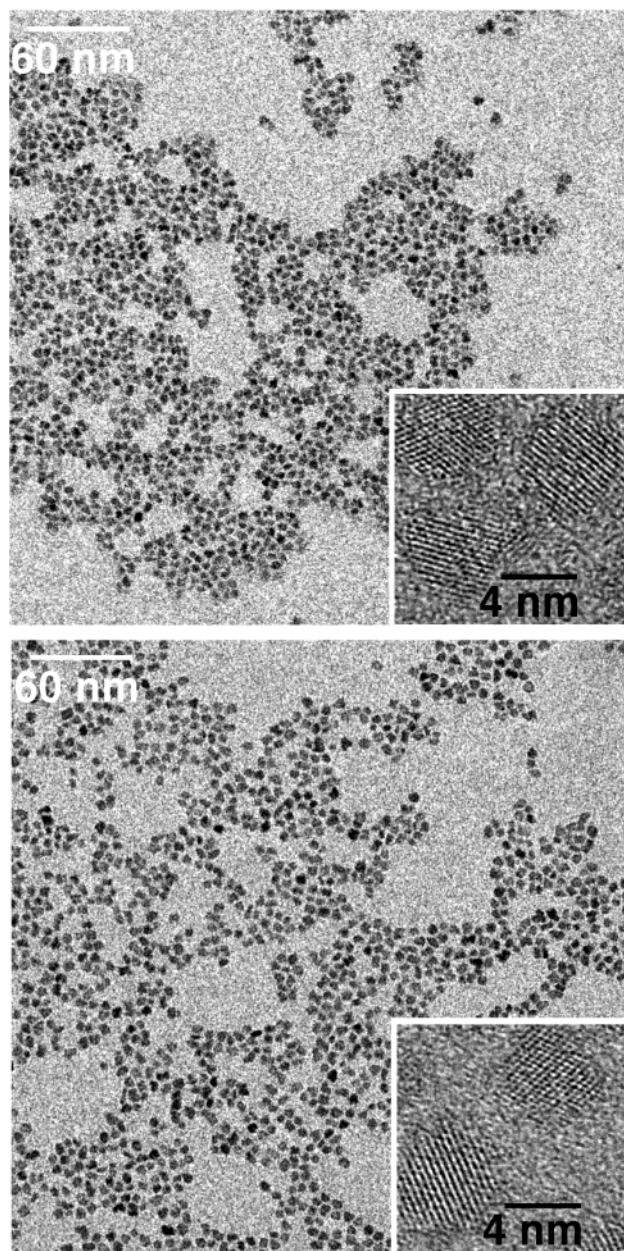


Figure 3. TEM micrographs of NdPO_4 nanoparticles (top) and YbPO_4 nanoparticles (bottom). Insets: High-resolution images of NdPO_4 nanoparticles and of YbPO_4 nanoparticles, respectively.

lutetium phosphate.^{9,10} Terbium phosphate at the border of the two phase regions is reported to be dimorphic.¹⁰ If the material is treated at high temperature for extended periods of time, then the monoclinic phase is usually obtained.

An inspection of the XRD pattern given in Figure 1 shows, however, that no such phase transition between gadolinium and dysprosium is observed for the nanoparticles. The X-ray diffraction patterns are very similar for all nanocrystalline phosphates from europium phosphate to holmium phosphate and are even more broadened than those of the other lanthanide phosphate particles. Although the diffractograms show some similarities to those of the monazite and the xenotime structure, they are in accord neither with the pattern expected for very small crystallites of monazite nor with that expected for very small xenotime particles.

The smaller particle size of these phosphates was already obvious when the crude products were purified and separated by diafiltration because 5000 Da filters were necessary to keep

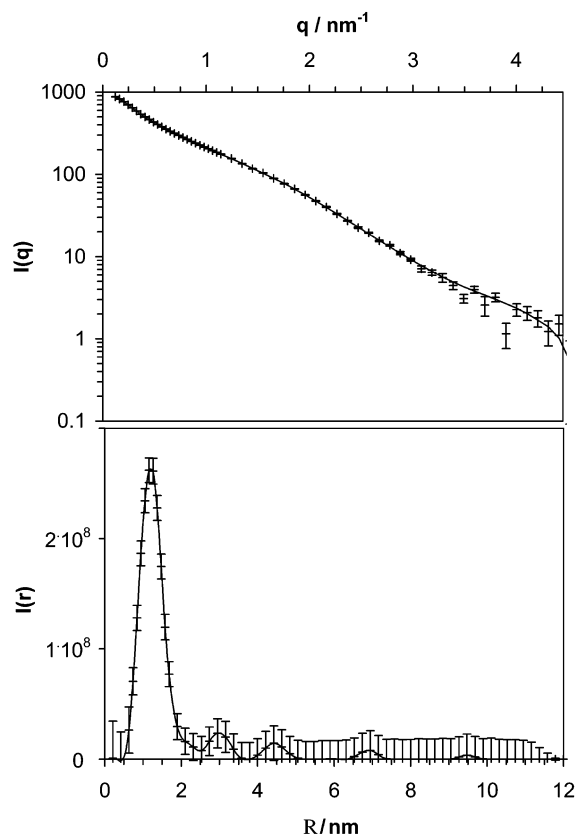


Figure 4. Top: Small-angle X-ray scattering (SAXS) curve of a colloidal solution of GdPO_4 nanoparticles in 2-propanol. The length of the scattering vector q is related to the scattering angle θ (i.e., the angle between the directions of incidence and detection) by $q = 4\pi/\lambda_0 \sin(\theta/2)$. Cu K α radiation was used ($\lambda_0 = 0.154$ nm). Bottom: Particle-size distribution deduced from the scattering curve by assuming spherical scatterers of radius R .

the nanoparticles inside the diafiltration cell. In contrast, phosphate nanoparticles of the lighter and the heavier lanthanides can be separated by using filters with a molecular weight cutoff of 10 000 Da (corresponding to a pore size of about 3 nm). Because TEM images of lanthanide phosphate nanoparticles with sizes below 3 nm suffer from low image contrast, the particle-size distribution in solution was measured by small-angle X-ray scattering (SAXS) as described earlier for 5-nm particles of doped (La, Ce) PO_4 .² The top portion of Figure 4 displays the scattering curve measured for gadolinium phosphate nanoparticles in 2-propanol, and the bottom part shows the corresponding particle-size distribution as calculated from the scattering curve. The peak width corresponds to a narrow particle-size distribution indicating redispersible particles that are well separated in solution. The position of the peak maximum in the distribution curve corresponds to a mean particle diameter as small as $2R = 2.6$ nm.

Despite their small size, these clusters are stable components that do not grow easily to larger nanoparticles. Even if heating of the reaction mixture is extended from 2 to 20 h, no particle growth is observed. The same holds true for the larger monazite and xenotime nanoparticles, indicating that Ostwald ripening (i.e., growth by the exchange of monomers between particles) is very weak under these reaction conditions. Thus, particle growth slows down drastically as soon as all reactants initially contained in the reaction mixture have been consumed.

The small mean particle size observed for europium, gadolinium, terbium, dysprosium, and holmium phosphate nanoparticles indicates either that this size is thermodynamically more

stable than other sizes or that the ratio between the nucleation rate and the growth rate is larger for these materials than for the other lanthanides. According to classical nucleation theory, the total free energy of a crystallite contains one term that is proportional to the surface area of the crystallite and a second term that is proportional to the volume of the crystallite. In the case of surface-capped nanoparticles, the surface term will strongly depend on the number, the spatial arrangement, and the binding of surface ligands whereas the "bulk" term will depend on the lattice energy of the corresponding bulk crystal phase. Close to the phase-transition point, the lattice energies of the monoclinic monazite phase and the tetragonal xenotime phase are very similar. A small energy difference between two crystal structures, however, can lead to lattice faults during the growth of small crystallites. For the case of hard-sphere colloids, for instance, where the energy difference between the face-centered cubic phase and the hexagonal close-packed phase is small, experiments have shown that small crystals always contain a large number of stacking faults.^{11,12} A recent numerical simulation by Auer and Frenkel¹³ indicates that the very small critical nuclei in hard-sphere colloids are even randomly stacked and that the origin of this random stacking is not purely kinetic, as usually assumed, but that, in the early stages of nucleation, the randomly stacked structure is the most stable.

Compared to hard-sphere colloids, our systems are more complicated because the phase transition goes from monoclinic to tetragonal and because the surfaces of our nanoparticles are capped by organic ligands. For small clusters, where the contribution of the surface term to the total free energy is considerable, it has been shown that the choice of the organic ligand can determine the whole crystal structure of the cluster core.¹⁴ A beautiful example is ligand-capped $(\text{Cu}_2\text{S})_{22}$ clusters that are obtained in two different structural isomers depending on the choice of phosphine ligand used in the synthesis.¹⁵ Because clusters of both isomers self-organize into 3D superlattices, the latter of which form comparatively large crystals, the authors were able to solve the structures of both isomers by single-crystal X-ray analysis. Their analysis shows that the trialkylphosphine ligands of these clusters bind to copper atoms at the surface of the cluster core. Moreover, it is found that the positions of these copper atoms depend on the positions of the phosphine ligands at the surface and that the positions of the phosphine ligands are determined by the spatial requirements of their alkyl groups. Because the positions of the surface atoms in turn influence the positions of atoms inside the cluster core, the whole structure of the small $(\text{Cu}_2\text{S})_{22}$ clusters depends on the choice of the phosphine ligand.¹⁵

This structure-determining mechanism of the capping molecules can work well only if the energy gained by the formation of an energetically favorable arrangement of molecules in the ligand shell is not overcompensated for by the additional energy required to move atoms of the cluster core to lattice positions with higher energy. Close to the border of the phase transition from monoclinic to tetragonal, it is probable that the energy of atoms occupying surface sites that correspond to the monoclinic phase is not very different from the energy of those occupying sites of the tetragonal lattice. Therefore, a larger number of surface sites with similar energy may be available. Consequently, an energetically favorable spatial arrangement of the ligands can be achieved for systems close to the phase transition because the surface atoms that bind to these ligands can occupy nonstandard surface sites without increasing the total energy of the system too much.

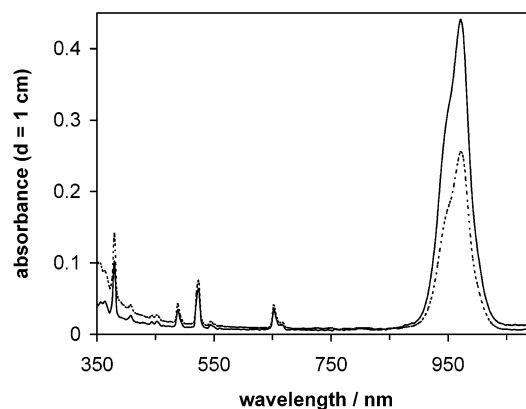


Figure 5. UV-vis-NIR absorption spectra of colloidal solutions of YbPO_4/Er (—) and $\text{LuPO}_4/\text{Yb, Er}$ (···), both solutions containing about 1 wt % of nanoparticles.

In fact, the structure of the small phosphate nanoparticles around terbium is more strongly influenced by decomposition reactions of the capping agent than all of the other lanthanide phosphate nanoparticles. Decomposition reactions of the capping agent tributyl phosphate occur if heating of the reaction mixture at 200 °C is extended for several days, but this only weakly affects the larger monazite and xenotime nanoparticles. Although the amount of capping agent employed in the synthesis discussed here is significantly smaller as compared to the amount in our previous recipes, colloids of cerium, praseodymium, neodymium, and samarium phosphate as well as colloids of erbium, thulium, ytterbium, and lutetium phosphate do not show an agglomeration of particles even after heating the reaction mixture for 3 days. TEM images of these systems show well-separated particles with the mean particle size being increased by no more than 20%. In contrast, reaction mixtures containing small clusters of europium, gadolinium, terbium, dysprosium, or holmium phosphate become turbid after heating at 200 °C for only 2 days, and TEM images of the resulting products show inhomogeneous mixtures containing a very broad size distribution of nanoparticles and nanoparticle agglomerates. An analysis of the XRD data shows that in the cases of europium phosphate and gadolinium phosphate the products mainly consist of the monazite phase with an average domain size of about 15 to 20 nm. Similar average domain sizes are also observed for the main products in the cases of terbium, dysprosium, and holmium phosphate, but these products consist of a tetragonal phase. Although the details of this decomposition process remain to be further investigated, the results clearly indicate that the unique crystal structure of the small clusters is stable only below a certain critical size and/or as long as the shell of organic surface ligands is intact.

Moreover, these results indicate that chemical similarity may not be the only point to be considered when a synthesis procedure that is known to work well for a particular nanomaterial is adapted to the preparation of a new material. A strong influence may also be the proximity of the crystal structure of the new material to the next phase-transition border.

In the following, we present the first results of the luminescence of some of the new nanomaterials discussed above. In previous papers, we investigated the properties of Eu^{3+} , Ce^{3+} , and Tb^{3+} dopant ions in monazite-type LaPO_4 nanoparticles.^{2,3} Here we show that doping can also be achieved for 5-nm particles that crystallize in the tetragonal xenotime structure. Figure 5 displays the absorption spectra of colloidal solutions of dodecylamine-capped YbPO_4/Er and $\text{Lu}_{0.5}\text{Yb}_{0.5}\text{PO}_4/\text{Er}$ nanoparticles in toluene, both systems containing 5 atom % of erbium

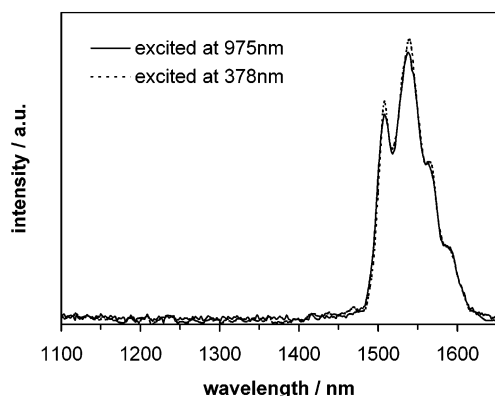


Figure 6. Er^{3+} luminescence of a colloidal solution of LuPO_4/Yb , Er nanoparticles measured at room temperature. (···) Upon excitation of the Er^{3+} ions at 378 nm. (—) Upon excitation of the Yb^{3+} ions at 975 nm.

with respect to the total metal content. The solutions are optically clear despite the high concentration of about 1 wt % of nanoparticles. Both spectra show a comparatively strong and broad absorption band at about 980 nm that is caused by the $^2\text{F}_{5/2}-^2\text{F}_{7/2}$ transition of ytterbium and a large number of additional weaker lines corresponding to f–f transitions of erbium. The absorption band at 980 nm is less intense for LuPO_4/Yb , Er because the ytterbium content of the crystal lattice is lower than in the case of the YbPO_4/Er colloid. Both colloids show Er^{3+} emission at about 1550 nm either via direct excitation of the erbium ions at 378 nm or after the excitation of the ytterbium ions at 980 nm. Figure 6 shows the emission spectra of the LuPO_4/Yb , Er colloid, which are identical to those observed for YbPO_4/Er . Obviously, energy transfer from Yb^{3+} to Er^{3+} takes place in both nanomaterials. This energy-transfer process is important for possible applications of these materials

because the absorption cross section of the ytterbium transition at 980 nm is much higher than that of the Er^{3+} transitions. Measurements of the luminescence lifetime and the quantum yield of the Er^{3+} emission are currently being performed and will be published elsewhere.

Acknowledgment. We thank Dr. D. Talapin and Dr. K.-H. Klaska for helpful discussions, A. Kornowski and S. Bartholdi-Nawrath for TEM investigations, and J. Ludwig for measuring X-ray powder diffractograms. This work was supported in part by the BMBF.

References and Notes

- (1) Hashimoto, N.; Takada, Y.; Sato, K.; Ibuki, S. *J. Lumin.* **1991**, *48*, 49, 893.
- (2) Riwotzki, K.; Meyssamy, H.; Schnablegger, H.; Kornowski, Haase, A. M. *Angew. Chem.* **2001**, *40*, 574. Riwotzki, K.; Meyssamy, H.; Schnablegger, H.; Kornowski, Haase, A. M. *Angew. Chem., Int. Ed.* **2001**, *40*, 573.
- (3) Meyssamy, H.; Riwotzki, K.; Kornowski, A.; Naused, S.; Haase, M. *J. Phys. Chem. B* **2000**, *104*, 2824.
- (4) Haase, M.; St. Haubold; Riwotzki, K.; Weller, H.; Meyssamy, H.; Ibarra, F. WO 02/20696 A1.
- (5) Hebbink, G. A.; Stouwdam, J. W.; Reinhoudt, D. N.; van Veggel, F. J. M. *Adv. Mater.* **2002**, *14*, 1147.
- (6) Glatter, O. *J. Appl. Crystallogr.* **1980**, *13*, 7.
- (7) Glatter, O. *Acta Phys. Austriaca* **1977**, *47*, 83.
- (8) Glatter, O. *J. Appl. Crystallogr.* **1977**, *10*, 415.
- (9) Ni, Y.-X.; Hughes, J. M.; Mariano, A. N. *Am. Mineral.* **1995**, *80*, 21.
- (10) Schwarz, H. Z. *Anorg. Allg. Chem.* **1963**, *323*, 45.
- (11) Zhu, J.; Li, M.; Rogers, R.; Meyer, W.; Ottewill, R. H. (STS-73 Space Shuttle Crew). Russel, W. B., Chalkin, P. M. *Nature* **1997**, *387*, 883.
- (12) Pusey, P. N. *Phys. Rev. Lett.* **1989**, *63*, 2753.
- (13) Auer, S.; Frenkel, D. *Nature* **2001**, *409*, 1020.
- (14) Dehnen, S.; Schäfer, A.; Fenske, D.; Ahlrichs, R. *Angew. Chem.* **1994**, *106*, 786. Dehnen, S.; Schäfer, A.; Fenske, D.; Ahlrichs, R. *Angew. Chem., Int. Ed. Engl.* **1994**, *33*, 746.
- (15) Dehnen, S.; Fenske, D. *Angew. Chem.* **1994**, *106*, 2369. Dehnen, S.; Fenske, D. *Angew. Chem., Int. Ed. Engl.* **1994**, *33*, 2287.